



## Article

**Cite this article:** Liu C *et al* (2020).

Measurements of turbulence transfer in the near-surface layer over the Antarctic sea-ice surface from April through November in 2016. *Annals of Glaciology* 61(82), 12–23. <https://doi.org/10.1017/aog.2019.48>

Received: 6 February 2019

Revised: 9 December 2019

Accepted: 10 December 2019

First published online: 9 January 2020

**Key words:**

Aerodynamic roughness length; Antarctic sea-ice surface; parameterization; scalar roughness length; surface energy budget; turbulent fluxes

**Author for correspondence:**

Zhiqiu Gao,

E-mail: [zgao@mail.iap.ac.cn](mailto:zgao@mail.iap.ac.cn) and

Qinghua Yang,

E-mail: [yangqh25@mail.sysu.edu.cn](mailto:yangqh25@mail.sysu.edu.cn)

# Measurements of turbulence transfer in the near-surface layer over the Antarctic sea-ice surface from April through November in 2016

Changwei Liu<sup>1</sup>, Zhiqiu Gao<sup>2,3</sup>, Qinghua Yang<sup>4,5</sup> , Bo Han<sup>4</sup>, Hong Wang<sup>2</sup>, Guanghua Hao<sup>6</sup>, Jiechen Zhao<sup>7</sup>, Lejiang Yu<sup>7</sup>, Linlin Wang<sup>3</sup> and Yubin Li<sup>2</sup>

<sup>1</sup>Collaborative Innovation Centre on Forecast and Evaluation of Meteorological Disasters, School of Remote Sensing and Geomatics Engineering, Nanjing University of Information Science and Technology, Nanjing 210044, China; <sup>2</sup>Collaborative Innovation Centre on Forecast and Evaluation of Meteorological Disasters, School of Atmospheric Physics, Nanjing University of Information Science and Technology, Nanjing 210044, China; <sup>3</sup>State Key Laboratory of Atmospheric Boundary Layer Physics and Atmospheric Chemistry, Institute of Atmospheric Physics, Chinese Academy of Sciences, Beijing 100029, China; <sup>4</sup>Guangdong Province Key Laboratory for Climate Change and Natural Disaster Studies, School of Atmospheric Sciences, Sun Yat-sen University, Zhuhai 519000, China; <sup>5</sup>Southern Marine Science and Engineering Guangdong Laboratory (Zhuhai), Zhuhai 519000, China; <sup>6</sup>National Marine Environmental Forecasting Center, Beijing 100081, China and <sup>7</sup>SOA Key Laboratory for Polar Science, Polar Research Institute of China, Shanghai 200129, China

**Abstract**

The surface energy budget over the Antarctic sea ice from 8 April 2016 through 26 November 2016 are presented. From April to October, Sensible heat flux ( $SH$ ) and subsurface conductive heat flux ( $G$ ) were the heat source of surface while latent heat flux ( $LE$ ) and net radiation flux ( $R_n$ ) were the heat sink of surface. Our results showed larger downward  $SH$  (due to the warmer air in our site) and upward  $LE$  (due to the drier air and higher wind speed in our site) compared with SHEBA data. However, the values of  $SH$  in N-ICE2015 campaign, which located at a zone with stronger winds and more advection of heat in the Arctic, were comparable to our results under clear skies. The values of aerodynamic roughness length ( $z_{0m}$ ) and scalar roughness length for temperature ( $z_{0h}$ ), being  $1.9 \times 10^{-3}$  m and  $3.7 \times 10^{-5}$  m, were suggested in this study. It is found that snow melting might increase  $z_{0m}$ . Our results also indicate that the value of  $\log(z_{0h}/z_{0m})$  was related to the stability of stratification. In addition, several representative parameterization schemes for  $z_{0h}$  have been tested and a couple of schemes were found to make a better performance.

**1. Introduction**

The surface fluxes over sea ice influence the mass balance and drift direction of sea ice (e.g. Vihma and others, 2009). Such studies in Polar Regions have been attracting great attention, due to its strong effect to the regional and global climate (e.g. King and others, 1996, 2001; Reijmer and others, 2003; Bourassa and others, 2013). However, very limited observations of radiative and turbulent characteristics have been performed over the Antarctic sea ice (e.g. Vihma and others, 2009; Weiss and others, 2011; Yu and others, 2019), while most in situ studies of surface radiation and turbulent fluxes in Polar seas have been carried out in the Arctic to date (e.g. Perovich and others, 2002; Schröder and others, 2003; Grachev and others, 2007; Perovich and Polashenski, 2012; Walden and others, 2017). Furthermore, most existing observational records over the Antarctic sea ice are either too short or do not involve all surface energy budget components. With these limited observations, the sea-ice conditions around Antarctica were found to be quite different from the Arctic (Wendler and others, 2000).

To find the mechanism controlling the variation of sea-ice thickness in the Antarctic region, a proper estimation of surface heat fluxes over sea ice was crucial (Vihma and others, 2009; Lazzara and others, 2012). Because of the rareness of directly turbulent observation, surface energy budget over sea ice in the Antarctic region was studied mainly by using numerical models (Andreas and others, 1984; Andreas, 1987; Stearns and Weidner, 1993; King and others, 1996, 2001). Previous studies show that Monin-Obukhov similarity theory (MOST) is applicable from unstable to stable conditions in Polar Regions (e.g. Garratt, 1992; Rodrigo and Anderson, 2013; Liu and others, 2019), although some limitations exist when the gradient Richardson number is larger than  $\sim 0.2$ – $0.25$  (Grachev and others, 2013). Before using these MOST-based models to estimate surface turbulent fluxes over sea ice, the real surface energy budget status as well as some crucial parameters, such as roughness lengths, must be ascertained or verified from observation (Munro, 1989; King and others, 1990; Yagüe and Cano, 1994; Cassano and others, 2001; Cullen and others, 2007; Vignon and others, 2017).

Previous studies have found that roughness lengths over ice surface are  $\sim 10^{-5}$ – $10^{-2}$  m, which are affected by the local morphology, melting and snowdrifting (King and Anderson, 1994; Bintanja and Van den Broeke, 1995; Van den Broeke and others, 2005; Guo and others, 2011). Based on the laboratory and field data, Andreas (1987) proposed a surface-renewal

© The Author(s) 2020. This is an Open Access article, distributed under the terms of the Creative Commons Attribution licence (<http://creativecommons.org/licenses/by/4.0/>), which permits unrestricted re-use, distribution, and reproduction in any medium, provided the original work is properly cited.

model to relate the aerodynamic roughness length ( $z_{0m}$ ) and the scalar roughness length for temperature ( $z_{0h}$ ) over snow and ice surface, and the model was further modified by Smeets and Van den Broeke (2008b) over a rougher surface. In the surface-renewal model,  $kB^{-1} [\equiv \log(z_{0m}/z_{0h})]$  was parameterized with friction velocity ( $u_*$ ) and  $z_{0m}$ . Nevertheless, studies show that, over vegetated land surface, thermal conditions also impact  $kB^{-1}$  and lead to a diurnal variation (e.g. Sun, 1999; Rigden and others, 2018), while Yang and others (2002 and 2007) proposed a temperature scale ( $T_*$ ) dependent model to calculate  $kB^{-1}$  over the surface covered by bare soil or partially covered by very short vegetation. On the other hand, Brunke and others (2006) indicated that there was no evident dependence of  $z_{0h}$  on surface temperature or friction velocity and suggested a constant  $z_{0h}$  of  $5 \times 10^{-4}$  m for sea-ice surface in the Arctic region. It is obvious that the parameterization for  $z_{0h}$  remains unsolved owing to natural complexities of air–sea-ice surface interaction in the Antarctic region.

This paper concentrates on the evolution of surface energy components and the parameterization of roughness lengths by using the data collected at an Antarctic sea ice station from 8 April 2016 through 26 November 2016. To our best knowledge, this observation is the longest direct measurement of latent heat flux by using eddy covariance technology over the Antarctic sea-ice surface. The main objective of this paper is to obtain data that can form a basis for better parameterization of eddy fluxes in mesoscale weather and large-scale climate models for this particular geographical area. To achieve this objective, this paper is organized as follows: material and methods are described in Section 2. In Section 3, we present the results and discussion about the conventional meteorological conditions, characteristics of radiative and turbulent fluxes, and roughness lengths parameterization. At last, conclusions are given in Section 4.

## 2. Material and methods

### 2.1 Site and instruments

The observation site was located at a fixed landfast sea ice of East Antarctica, at  $69^{\circ}22'08.1''S$ ,  $76^{\circ}21'42.1''E$ , and east of Amery ice shelf, northwest of Princess Elizabeth land, south of the Prydz bay (Fig. 1a). It is  $\sim 260$  m from the nearest sea-ice edge (adjacent to land) and within 5 km from the nearest glacier on Princess Elizabeth land. During the observation period, the sea-ice thickness gradually increased from 0.5 m in April to 1.8 m in November with a mean value of 1.3 m. The mean snow thickness was 0.13 m, and the largest (smallest) monthly mean snow thickness of 0.35 (0.07) m occurred in July (November). A mast was installed on sea-ice surface, typically covered by snow, and the instruments on the mast included (Fig. 1c): an infrared radiometer SI-111, a net radiometer CNR4, a temperature and humidity sensor HMP155, a three-dimensional (3-D) sonic anemometer CSAT3B, and an in situ, open-path, mid-infrared gas ( $CO_2/H_2O$ ) analyzer integrated with a 3-D sonic anemometer IRGASON. The IRGASON is controlled by the EC100 electronics, which uses inputs from a temperature thermistor probe 107 and a barometer CS106. The key technical specifications and installation height of these instruments can be found in Table 1. Additionally, the precipitation, which reported as snow water equivalent, used in this study is from the Russian Progress II station (located  $\sim 1$  km from Zhongshan station). Consecutive observations were carried out from 8 April 2016 through 26 November 2016. Except for precipitation data, all the data were averaged every half hour, and data processing and quality control were carried out as follows:

- (1) The spikes in the data series were removed by using a criterion of  $X(t) < (\bar{X} + 4\sigma)$  or  $X(t) > (\bar{X} + 4\sigma)$ , where  $X(t)$  denotes the measurements,  $\bar{X}$  is the mean over the interval and  $\sigma$  is the Std dev..
- (2) Surface turbulent fluxes were calculated by the eddy covariance method with 30 min averaging period. Turbulent data processing includes linear detrending, coordinate rotation, frequency correction, virtual temperature correction for sensible heat flux ( $SH$  hereafter) and WPL correction for latent heat flux ( $LE$  hereafter) (Lee, and others, 2004).
- (3) Data quality control for eddy covariance measurements includes nonstationarity test, integrated turbulence characteristics test and horizontal wind angle test. After these three tests, the data are classified into nine grades. Foken and others (2012) suggested that classes 1–3 can be used for fundamental research, such as the development of parameterizations. Hence, only classes 1–3 of data were chosen in our research.

Additionally, the data in the sector of wind direction ranged from  $65^{\circ}$  to  $115^{\circ}$ , which account for 75% of total data (Fig. 2), were chosen to do footprint analysis by using the Kljun and others (2015) model. From Figure 1b, it can be seen that 90% of the measured flux was expected to come from within 250 m of the observation site. Within this fetch, it is entirely sea-ice surface.

### 2.2 Eddy covariance (EC) methods

EC method uses the turbulent fluctuations of meteorological elements measured by high frequency observation instruments to calculate surface turbulent fluxes,

$$\tau = -\overline{\rho w' u'}, \quad (1)$$

$$SH = \overline{\rho c_p w' \theta'}, \quad (2)$$

$$LE = \lambda \overline{\rho w' q'}, \quad (3)$$

where,  $\tau$  ( $N m^{-2}$ ) is the turbulent momentum flux,  $w'$  ( $m s^{-1}$ ),  $u'$  ( $m s^{-1}$ ),  $\theta'$  (K), and  $q'$  ( $kg kg^{-1}$ ) are the turbulent fluctuations of vertical velocity, horizontal velocity, potential temperature and specific humidity, respectively,  $\rho$  ( $kg m^{-3}$ ) is the air density,  $c_p$  ( $J kg^{-1} K^{-1}$ ) is the constant-pressure specific heat capacity of air and  $\lambda$  ( $J kg^{-1}$ ) is the latent heat of vaporization.  $c_p$  and  $\lambda$  can be calculated from Eqn (4) and (5),

$$c_p = (c_{pd}\rho_d + c_{pw}\rho_w)/(\rho_d + \rho_w), \quad (4)$$

$$\lambda = [2501 - 2.365 \times (T_a - 273.15)] \times 1000, \quad (5)$$

where,  $c_{pb}$  ( $= 1004 J kg^{-1} K^{-1}$ ) and  $c_{pw}$  ( $= 1952 J kg^{-1} K^{-1}$ ) are the specific heat of dry and water vapor at constant pressure, respectively,  $\rho_d$  ( $kg m^{-3}$ ) and  $\rho_w$  ( $kg m^{-3}$ ) are the density of dry air and water vapor, respectively,  $T_a$  (K) is the air temperature.

### 2.3 Bulk method

In the context of MOST, surface turbulent fluxes can be parameterized as,

$$\tau = \rho u_*^2, \quad (6)$$

$$SH = -\rho c_p u_* T_*, \quad (7)$$

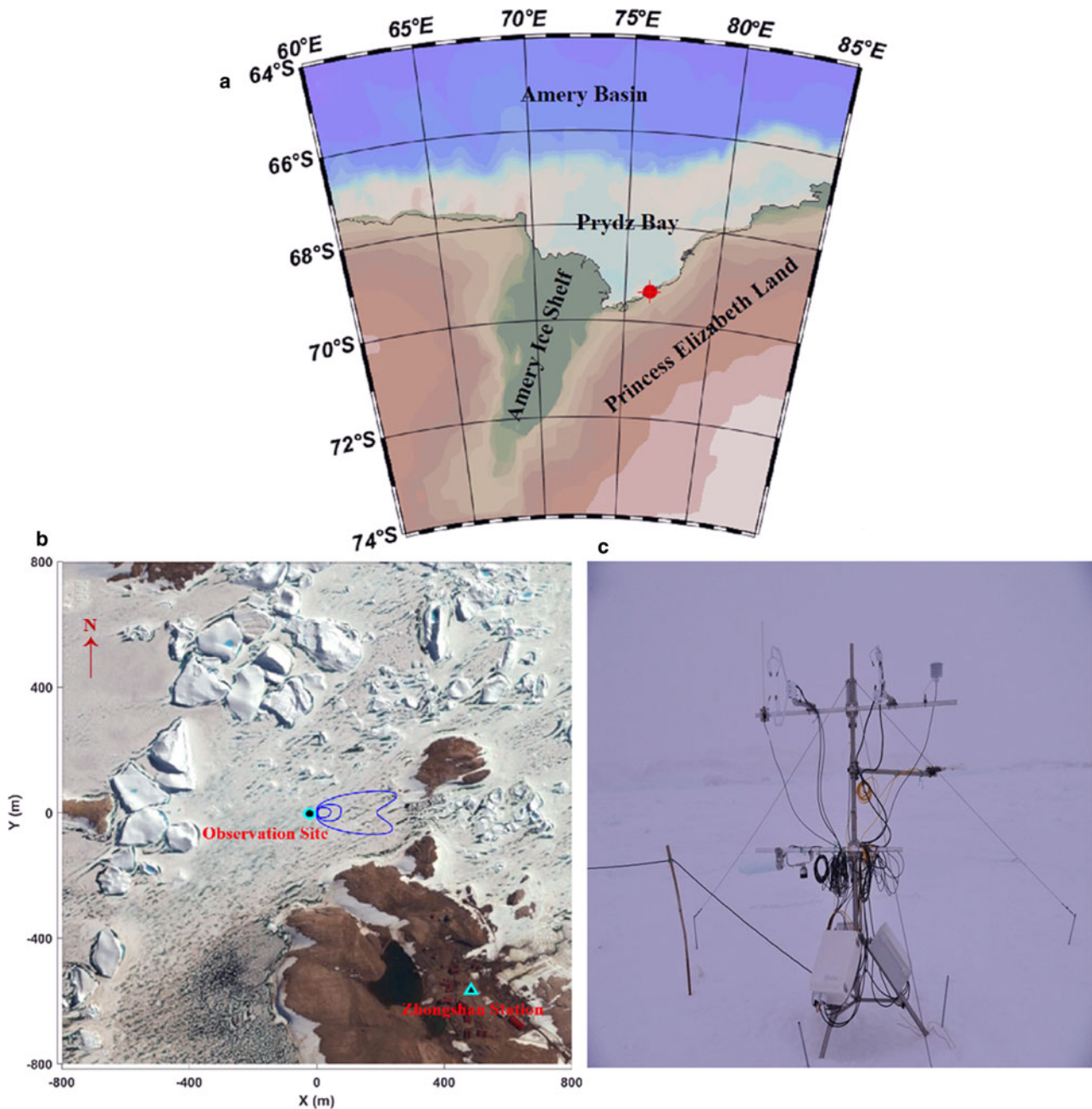


**Fig. 1.** (a) The geographical location of observation site (the red dot), (b) the local topography and sketch of footprint with 50, 70, and 90% flux source areas (the blue circles), and (c) the meteorological tower at observation site.

$$LE = -\lambda\rho u_* q^*,$$

$$u_* = \frac{uk}{[\ln(z/z_{0m}) - \psi_M(z/L) + \psi_M(z_{0m}/L)]},$$

$$T_* = \frac{(T_a - T_s)k}{R[\ln(z/z_{0h}) - \psi_H(z/L) + \psi_H(z_{0h}/L)]},$$

$$q^* = \frac{(q_a - q_s)k}{R[\ln(z/z_{0q}) - \psi_E(z/L) + \psi_E(z_{0q}/L)]},$$

$$L \equiv \frac{u_*^2 T_a}{kgT_*},$$

- (8) where,  $u_*$  ( $\text{m s}^{-1}$ ),  $T_*$  (K), and  $q^*$  ( $\text{kg kg}^{-1}$ ) are the frictional velocity, temperature scale, and specific humidity scale, respectively,  $u$  ( $\text{m s}^{-1}$ ) is the horizontal velocity,  $k$  ( $= 0.4$ ) is the von Kármán constant,  $z$  (m) is the observation height,  $z_{0m}$  (m),  $z_{0h}$  (m), and  $z_{0q}$  (m) are the aerodynamic roughness length, scalar roughness length for temperature and scalar roughness length for vapor water, respectively,  $L$  (m) is the Obukhov length,  $T_s$  (K) is the surface temperature,  $q_a$  ( $\text{kg kg}^{-1}$ ) and  $q_s$  ( $\text{kg kg}^{-1}$ ) are the specific humidity at observation height and surface, respectively,  $R$  is the Prandtl number,  $g$  ( $= 9.8 \text{ m s}^{-2}$ ) is the gravitational constant, and  $\psi_M$ ,  $\psi_H$  and  $\psi_E$  are the integrated stability correction functions for wind, temperature and humidity, respectively. Because  $z_{0q}$  and  $\psi_E$  are difficult to determine, the usual practice is to assume that  $z_{0q} = z_{0h}$  and  $\psi_E = \psi_H$ . Therefore, this paper will focus on the parameterization of  $\tau$  and  $SH$ .
- (9)
- (10)
- (11)
- (12) Stability correction functions and roughness lengths are two key issues in the Bulk method. Following stability correction

**Table 1.** The type of sensors and their key technical specifications

Sensor type	Measurement range	Precision	Sampling frequency	Installation height
SI-111	$T_s$ : $-40 \sim +80^\circ\text{C}$	$\pm 0.5^\circ\text{C}$	0.1 Hz	1 m
CNR4	$S_{\downarrow}, S_{\uparrow}$ : $0 \sim 2000 \text{ W m}^{-2}$ $L_{\downarrow}-L_{\uparrow}$ : $-250 \sim +250 \text{ W m}^{-2}$	Daily totals: $\pm 10\%$ Daily totals: $\pm 10\%$	0.1 Hz	1.5 m
HMP155	$T_a$ : $-80 \sim +60^\circ\text{C}$ $RH$ : $0.8 \sim 100\%$	$\pm(0.226-0.0028 \times T_a)^\circ\text{C}$ in $-80 \sim +20^\circ\text{C}$ $\pm(0.055+0.0057 \times T_a)^\circ\text{C}$ in $+20 \sim +60^\circ\text{C}$ $\pm(1.4+0.032 \times RH)\%$ in $-60 \sim -40^\circ\text{C}$ $\pm(1.2+0.012 \times RH)\%$ in $-40 \sim -20^\circ\text{C}$ $\pm(1+0.008 \times RH)\%$ in $-20 \sim +40^\circ\text{C}$ $\pm(1.2+0.012 \times RH)\%$ in $+40 \sim +60^\circ\text{C}$	0.1 Hz	2 m
CSAT3B	$u, v$ : $-60 \sim +60 \text{ m s}^{-1}$ $w$ : $-8 \sim +8 \text{ m s}^{-1}$ $T_v$ : $-50 \sim +60^\circ\text{C}$	$u, v$ : $\pm 0.08 \text{ m s}^{-1}$ $w$ : $\pm 0.04 \text{ m s}^{-1}$ $T_v$ : $\pm 0.025^\circ\text{C}$	10 Hz	2 m
IRGASON	$u$ : $-30 \sim +30 \text{ m s}^{-1}$ $v$ : $-60 \sim +60 \text{ m s}^{-1}$ $w$ : $-8 \sim +8 \text{ m s}^{-1}$ $T_v$ : $-50 \sim +60^\circ\text{C}$ $q$ : $0 \sim 72 \text{ mmol mol}^{-1}$ $\text{CO}_2$ : $0 \sim 1000 \mu\text{mol mol}^{-1}$	$u, v$ : $\pm 0.08 \text{ m s}^{-1}$ $w$ : $\pm 0.04 \text{ m s}^{-1}$ $T_v$ : $\pm 0.025^\circ\text{C}$ $q$ : $\pm 0.004 \text{ g m}^{-3}$ $\text{CO}_2$ : $\pm 0.2 \text{ mg m}^{-3}$	10 Hz	2 m
107	$T_a$ : $-35 \sim +50^\circ\text{C}$	$\pm 0.2^\circ\text{C}$	0.1 Hz	2 m
CS106	$P_a$ : $500 \sim 1100 \text{ hPa}$	$\pm 1.5 \text{ hPa}$ in $-40 \sim +60^\circ\text{C}$	0.1 Hz	0.5 m

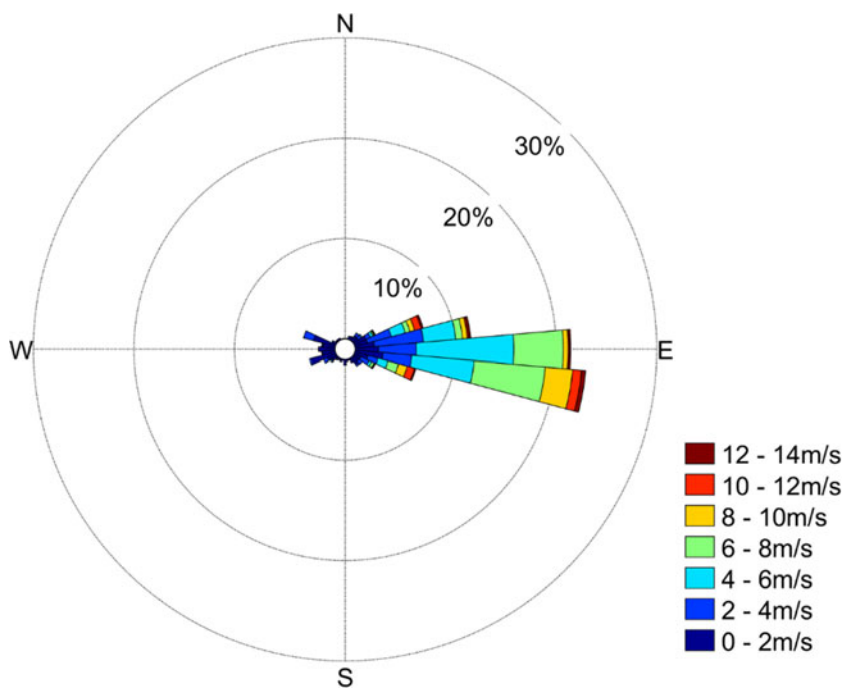


**Fig. 2.** Wind rose during the period from 8 April 2016 through 26 November 2016 at observation site.

functions for unstable stratification proposed by Cheng and Brutsaert (2005) and for stable stratification suggested by Paulson (1970) are used in this study,

$$\psi_M(\zeta) = \ln \left[ \left( \frac{1+x}{2} \right)^2 \left( \frac{1+x^2}{2} \right) \right] - 2 \arctan(x) + \frac{\pi}{2} \text{ (for unstable stratification),} \quad (13)$$

$$\psi_H(\zeta) = 2 \ln \left( \frac{1+y}{2} \right) \text{ (for unstable stratification),} \quad (14)$$

$$\psi_M(\zeta) = -a \ln[\zeta + (1 + \zeta^b)^{1/b}] \text{ (for stable stratification),} \quad (15)$$

$$\psi_H(\zeta) = -c \ln[\zeta + (1 + \zeta^d)^{1/d}] \text{ (for stable stratification),} \quad (16)$$

where,  $\zeta (=z/L)$  is the stability parameter,  $x=(1-16\zeta)^{1/4}$  and  $y=(1-16\zeta)^{1/2}$ ,  $a=6.1$ ,  $b=2.5$ ,  $c=5.3$ , and  $d=1.1$ .

For roughness lengths, Andreas (1987, hereafter as A87) proposed a theoretical model that predicts  $z_{0h}$  over ice surface from roughness Reynolds number ( $Re_*$ ),

$$\ln \left( \frac{z_{0h}}{z_{0m}} \right) = b_0 + b_1[\ln(Re_*)] + b_2[\ln(Re_*)]^2, \quad (17)$$

$$Re_* = \frac{u_* z_{0m}}{\nu}, \quad (18)$$

where  $\nu (=1.53 \times 10^{-5} \text{ m}^2 \text{ s}^{-1})$  is the air kinematic viscosity. The polynomial coefficients  $b_0$ ,  $b_1$  and  $b_2$  are listed in Table 2. By using the data collected during the experiments in Greenland and Iceland, Smeets and Van den Broeke (2008b, hereafter as S08) updated the polynomial coefficients for  $z_{0h}$  in Eqn (17). In addition, Zilitinkevich (1995) proposed a simple Reynolds number-

**Table 2.** Values of the polynomial coefficients for  $z_{0h}$  in Eqn (13)

	Smooth	Rough	
A87	$Re_* \leq 0.135$	$0.135 < Re_* < 2.5$	$2.5 \leq Re_* < 1000$
$b_0$	1.250	0.149	0.317
$b_1$	0	-0.550	-0.565
$b_2$	0	0	-0.183
S08	$z_{0m} < 10^{-3}$	$z_{0m} > 10^{-3}$	
$b_0$	0.317	1.5	
$b_1$	-0.565	-0.2	
$b_2$	-0.183	-0.11	

dependent formulation for all kinds of surface,

$$\ln\left(\frac{z_{0h}}{z_{0m}}\right) = -kC\sqrt{Re_*}, \quad (19)$$

where  $C$  is an empirical constant and is equal to 0.8 in Zilitinkevich's study (hereafter as Z95). However, Chen and others (1997, hereafter as C97) suggested  $C$  with the value of 0.1 can reduce forecast precipitation bias by conducting the National Center for Environmental Prediction (NCEP) mesoscale Eta forecast model. In addition, to predict the diurnal variation of  $z_{0h}$ , Yang and others (2007, hereafter as Y07) proposed a formulation to calculate  $z_{0h}$  over the bare-soil surface,

$$z_{0h} = \left(\frac{70\nu}{u_*}\right) \times \exp(-\beta u_*^{0.5} |T_*|^{0.25}), \quad (20)$$

where  $\beta$  is a constant with the value of 7.2.

#### 2.4 Surface energy balance

In this study, the surface energy balance (SEB) of sea ice is written as (Persson and others, 2002; Else and others, 2014),

$$F_{\text{net}} = S_{\downarrow} + S_{\uparrow} + L_{\downarrow} + L_{\uparrow} + SH + LE + G, \quad (21)$$

where  $F_{\text{net}}$  is the total energy flux into surface slab,  $S_{\downarrow}$ ,  $S_{\uparrow}$ ,  $L_{\downarrow}$  and  $L_{\uparrow}$  are downward shortwave radiation flux, upward shortwave radiation flux, downward longwave radiation flux and upward longwave radiation flux, respectively.  $G$  is the subsurface conductive heat flux. The unit of energy components in Eqn (21) is  $\text{W m}^{-2}$ . In this SEB system, all terms on the right-hand side of Eqn (21) are defined positive when directed towards the surface.  $F_{\text{net}}$  may be positive or negative. The positive  $F_{\text{net}}$  indicates the snow or ice gains energy, which can be used to increase the temperature of surface slab, or melt when surface temperature is over melting point. The negative  $F_{\text{net}}$  means energy loss, and ice growth or cooling surface slab. The conductive heat flux in Eqn 21 can be estimated as,

$$G = -k_s[(T_s - T_{\text{ice}})/d_s] \text{ (surface with snow cover)} \quad (22)$$

or

$$G = -k_i[(T_s - T_w)/d_i] \text{ (surface with no snow cover)} \quad (23)$$

where,  $k_s$  ( $= 0.3 \text{ W m}^{-1} \text{ }^\circ\text{C}^{-1}$ ) and  $k_i$  ( $= 2 \text{ W m}^{-1} \text{ }^\circ\text{C}^{-1}$ ) are the thermal conductivity of snow and ice, respectively.  $T_{\text{ice}}$  is the ice surface temperature and  $T_w$  ( $= -1.8^\circ\text{C}$ ) is the water temperature at the bottom of the ice.  $d_s$  and  $d_i$  are snow and ice thickness, respectively. It is noted that the value of  $k_s$  is related to the physical properties of snowpack, for example snow density and humidity. Unfortunately, due to the lack of records of snow

physical properties, we have to use the value of  $0.3 \text{ W m}^{-1} \text{ }^\circ\text{C}^{-1}$  for  $k_s$ , which is typically used in large-scale sea-ice models (Toyota and others, 2011).

### 3. Results and discussion

#### 3.1 Conventional meteorological conditions

The easterlies prevailed during the whole observation period, as shown in Figure 2. The mean wind speed at 2 m height during the whole observation period was  $4.2 \text{ m s}^{-1}$ , and the 4-hour-averaged maximum value could reach  $13.9 \text{ m s}^{-1}$ . The largest (lowest) monthly mean wind speed of  $6.0$  ( $3.0$ )  $\text{m s}^{-1}$  occurred in August (July) (Fig. 3a). Especially, the wind speed in November showed a significant daily variation, which was related to the land-sea breeze. Figure 4a and 4b present the monthly mean diurnal variation of wind speed and wind direction in November, respectively. It can be seen that wind speed was higher in early morning and the monthly mean daily maximum wind speed reached  $7.9 \text{ m s}^{-1}$ , while the monthly mean daily minimum wind speed of  $1.4 \text{ m s}^{-1}$  appeared in the afternoon. The wind direction also showed a diurnal variation from east-south-easterlies in the morning to east-north-easterlies in the afternoon.

For temperature (Fig. 3b), the mean (4-hour-averaged maximum/minimum) air temperature at 2 m height during the whole observation period reached  $-15$  ( $3/-40$ ) $^\circ\text{C}$ . In contrast, the mean (4-hour-averaged maximum/minimum) surface temperature was a bit lower, being  $-17$  ( $2/-48$ ) $^\circ\text{C}$ . In November, the air temperature and surface temperature had clear diurnal variation, with monthly mean diurnal range of  $3.7$  and  $6.3^\circ\text{C}$ , respectively (Fig. 4c). The monthly mean daily maximum value of air temperature was close to that of surface temperature, but the monthly mean daily minimum value of air temperature and surface temperature was  $-4$  and  $-7^\circ\text{C}$  in November, respectively.

For relative humidity (Fig. 3c), the mean relative humidity at 2 m height during the whole observation period was 56%, and July (November) was the wettest (driest) month. For ambient air pressure (Fig. 3d), the mean ambient air pressure at 0.5 m height during the whole observation period was 978 hPa, and the lowest (highest) monthly mean ambient air pressure of 972 (986) hPa appeared in September (November). The total precipitation during the whole observation period was 156.9 mm, and concentrated in June (25.0 mm), July (44.1 mm) and October (24.2 mm). Figure 3f describes the variation of daily sunshine time and the sawteeth were caused by the sporadic clouds. It can be found that during the period from 7 May through 22 July was Polar night, and the monthly mean daily sunshine time reached 19 hours in November.

#### 3.2 Radiation fluxes

Figure 5 presents the monthly mean diurnal variation of  $S_{\downarrow}$ ,  $S_{\uparrow}$ ,  $L_{\downarrow}$ ,  $L_{\uparrow}$ ,  $R_n$  and albedo during the observation period. It can be seen from Figure 5a that there were significant differences in the monthly mean diurnal variation of  $S_{\downarrow}$  in different months. All days in June were Polar night, while the monthly mean daily maximum  $S_{\downarrow}$  reached  $659 \text{ W m}^{-2}$  in November. The monthly mean diurnal variation of  $S_{\uparrow}$  in different months also showed great distinctions, and the monthly mean daily maximum  $S_{\uparrow}$  reached  $-449 \text{ W m}^{-2}$  in November (Fig. 5b). For  $L_{\downarrow}$  and  $L_{\uparrow}$  (Fig. 5c and 5d), the largest (smallest) monthly mean absolute value of  $L_{\downarrow}$  and  $L_{\uparrow}$  were 227 and 296 (176 and 222)  $\text{W m}^{-2}$ , respectively, and both occurred in November (September). For  $R_n$  (Fig. 5e), there was a sharp diurnal variation in September, October and November, and the monthly mean daily maximum  $R_n$  in

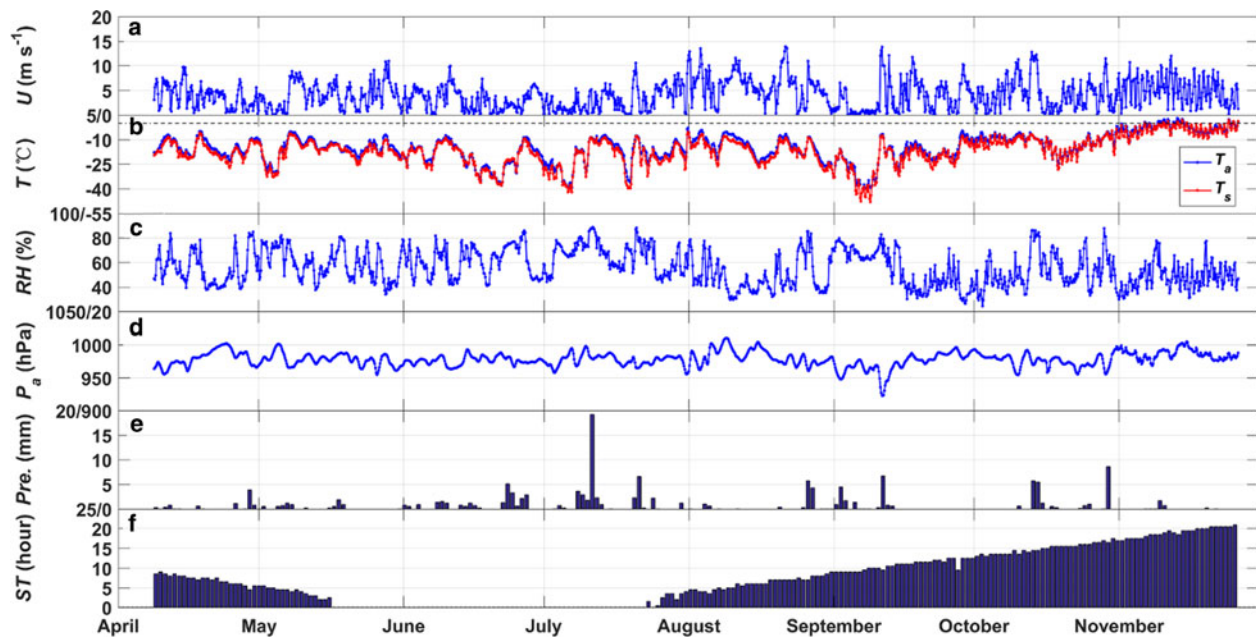


**Fig. 3.** Conventional meteorological data collected during the period from 8 April 2016 through 26 November 2016 at the observation site. (a), (b), (c), (d), (e) and (f) are the time series of 4-hourly average wind speed at 2 m height, air temperature (blue line) at 2 m height and surface temperature (red line), relative humidity at 2 m height, ambient air pressure at 0.5 m height, daily precipitation and daily sunshine time, respectively.

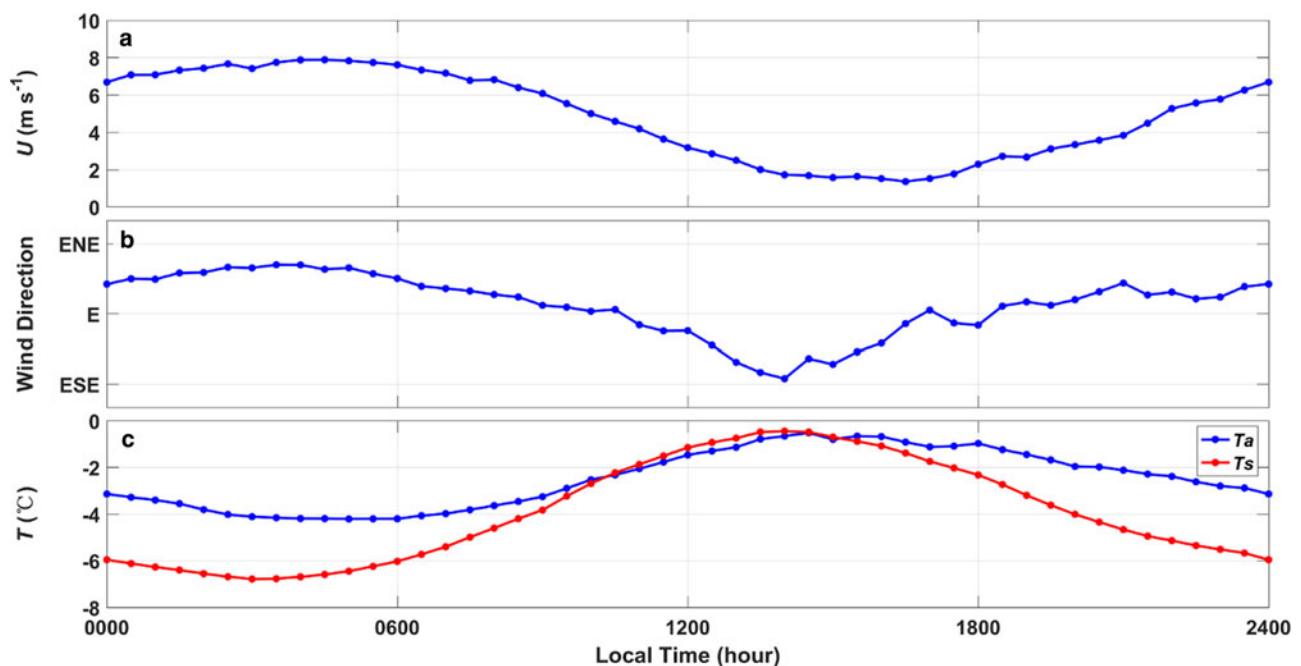


**Fig. 4.** The mean diurnal variation of (a) wind speed, (b) wind direction and (c) temperature (blue line for air temperature and red line for surface temperature) in November 2016.

September, October and November were  $-10$ ,  $42$  and  $136 \text{ W m}^{-2}$ , respectively. The positive monthly mean  $R_n$  only occurred in November, which was  $21 \text{ W m}^{-2}$ . The smallest monthly mean  $R_n$ ,  $-58 \text{ W m}^{-2}$ , appeared in August. From Figure 5f, the highest monthly mean albedo, being  $0.93$ , occurred in July. The albedo gradually decreased from July to October, reflecting the freezing process of accumulated snow (Yang and others, 2016). While melting process changed the properties of ice surface, making the monthly mean albedo in November much smaller ( $0.69$ ) than that in other months ( $>0.8$ ).

### 3.3 Turbulent fluxes and surface energy budget

The mean  $\tau$  during the whole observation period was  $0.15 \text{ N m}^{-2}$ , and the largest (smallest) monthly mean  $\tau$  of  $0.24$  ( $0.1$ )  $\text{N m}^{-2}$  occurred in August (July).  $\tau$  showed a significant monthly mean diurnal variation only in November (the pink line in Fig 6a), and the variation pattern was similar to that of the wind speed (Fig. 4a). The monthly mean daily maximum (minimum)  $\tau$  in this month was  $0.31$  ( $0.03$ )  $\text{N m}^{-2}$ . In November, because the surface snow around the observation site began to melt and the sea-ice area decreased, the thermal contrast between open ocean

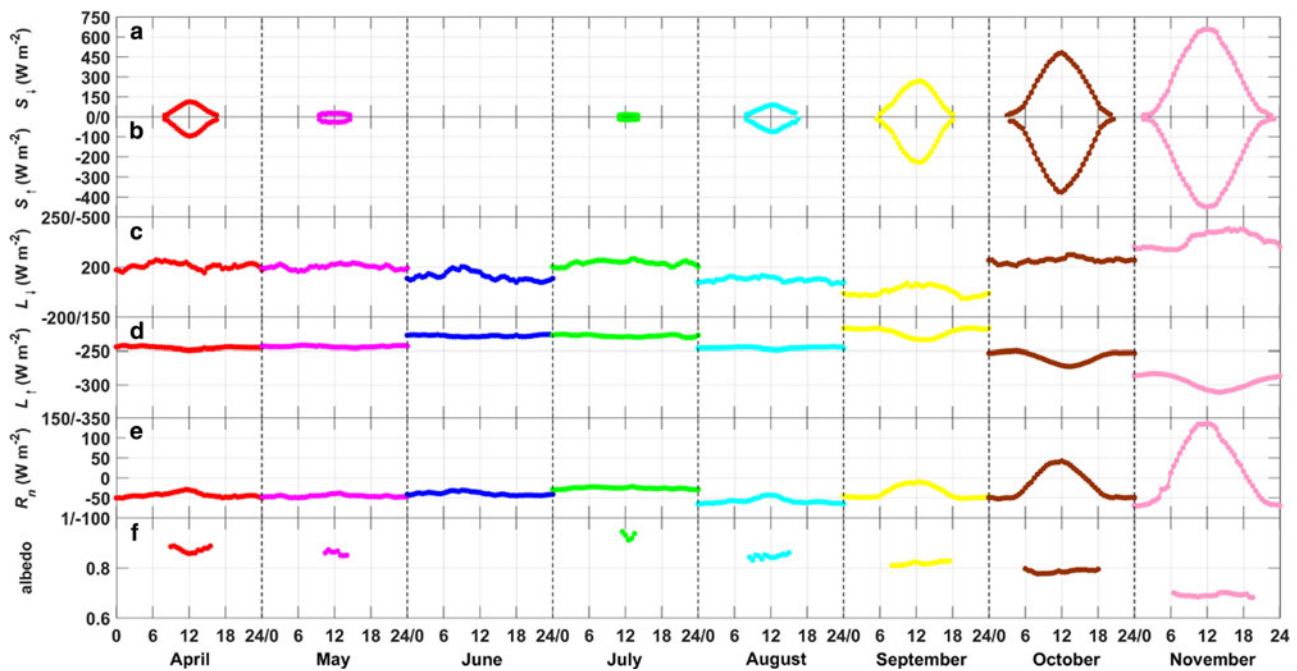


Fig. 5. The monthly mean diurnal variation of surface radiation fluxes and albedo during the observation period. (a), (b), (c), (d), (e) and (f) are the  $S_1$ ,  $S_2$ ,  $L_1$ ,  $L_2$ ,  $R_n$  and albedo, respectively.

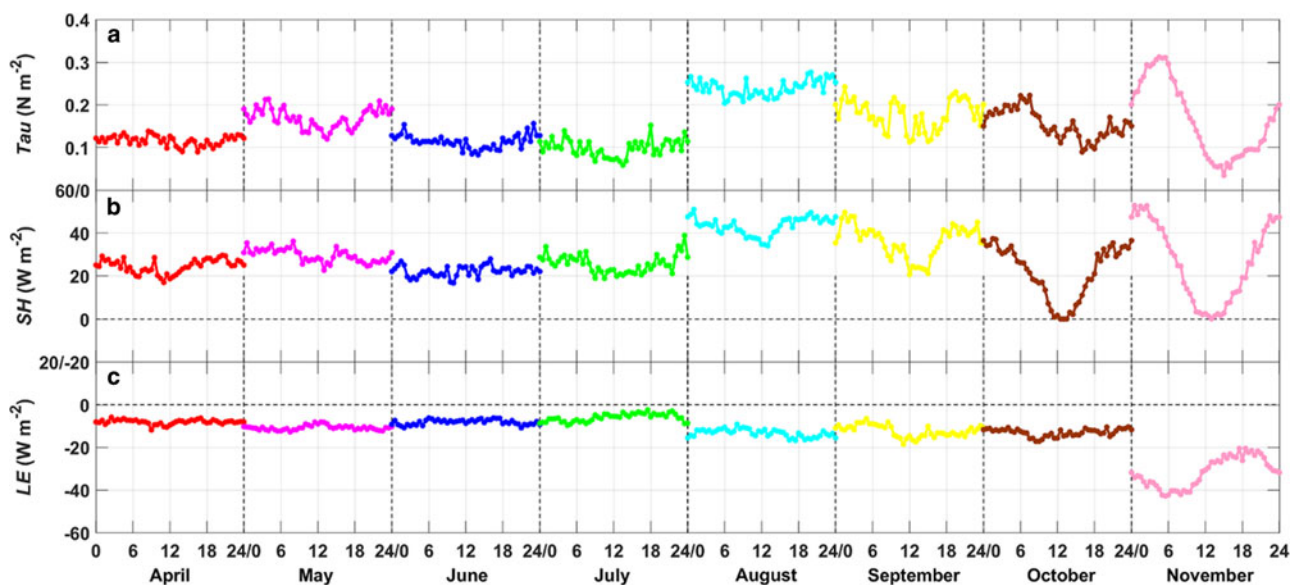


Fig. 6. The monthly mean diurnal variation of (a)  $\tau$  ( $Tau$ ), (b)  $SH$  and (c)  $LE$  during the observation period.

and land was intensified. Thus, a sea-land breeze might have modulated the near-surface wind and  $\tau$  near the site.

From Figure 6b, it can be found that the monthly mean  $SH$  was positive in each month during the observation period, which meant that the sea-ice surface generally absorbs sensible heat from atmosphere. The largest (smallest) monthly mean  $SH$  of 43 (21)  $W m^{-2}$  occurred in August (October). The mean value of  $SH$  in winter (June, July and August) was 31  $W m^{-2}$  that was significantly greater than that observed at the interior plateau ( $\sim 12 W m^{-2}$ ) and was similar to that observed at katabatic wind zone ( $\sim 32 W m^{-2}$ ) in Dronning Maud Land, East Antarctica (Van den Broeke and others, 2005). Our observation site is also located in katabatic wind zone, where strong winds frequently germinate. Van den Broeke and others (2005) indicated that the katabatic winds

vertically mix the air, which results in 5–10°C higher near-surface temperature than nonkatabatic wind region in Antarctica. Additionally, the warm signatures can also be found in katabatic wind region on satellite infrared imagery (King and others, 1998). So, strong wind conditions are conducive to the enhancement of downward  $SH$  in Antarctica. There was a clear monthly mean diurnal variation in  $SH$  with a diurnal range of 29, 37 and 53  $W m^{-2}$  in September, October and November, respectively (Fig. 6b). Contrary to  $SH$ , the monthly  $LE$  were negative in each month during the observation period (Fig. 6c), which meant that the sea-ice surface released mass to atmosphere through sublimation. The most significant sublimation appeared in November, with monthly mean  $LE$  of  $-32 W m^{-2}$ . The monthly mean diurnal variation of  $LE$  in November was obvious and was closely related to wind speed.

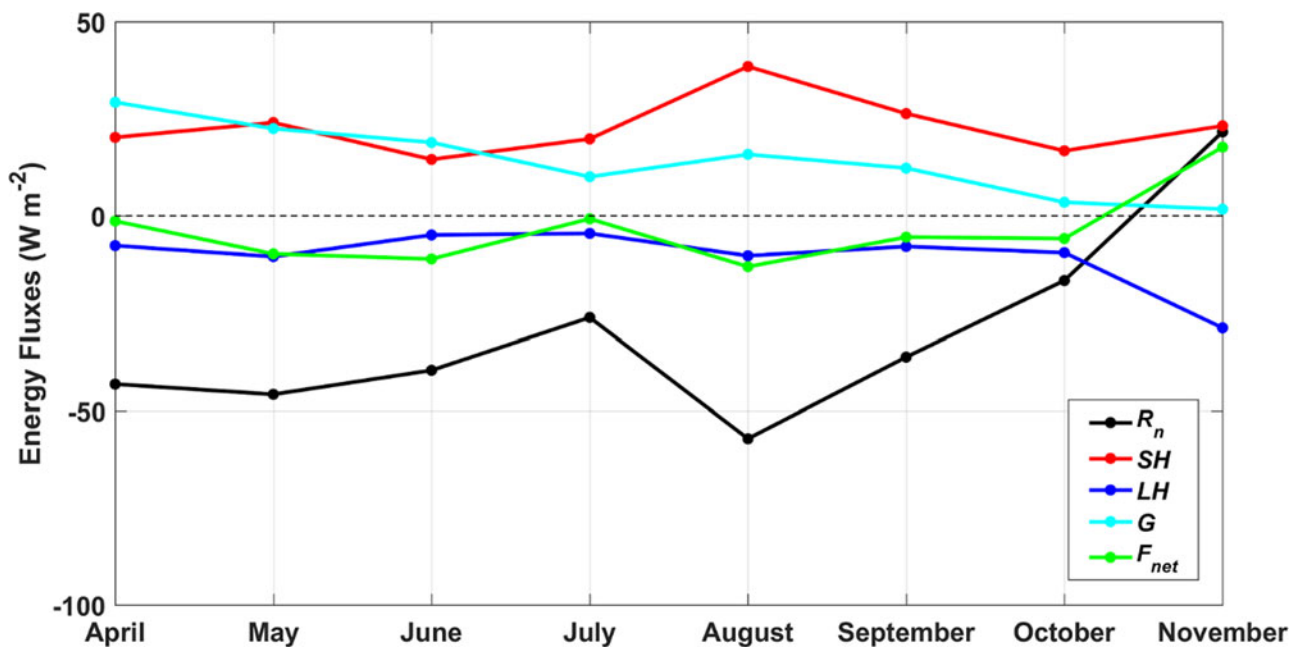


Fig. 7. The monthly variation of  $R_n$ ,  $SH$ ,  $LE$ ,  $G$  and  $F_{net}$  during the observation period.

Table 3. The monthly mean values of net shortwave radiation (NSR), net longwave radiation (NLR),  $R_n$ ,  $SH$ , and  $LE$  from November to May for our observation results and the values in brackets were results from SHEBA

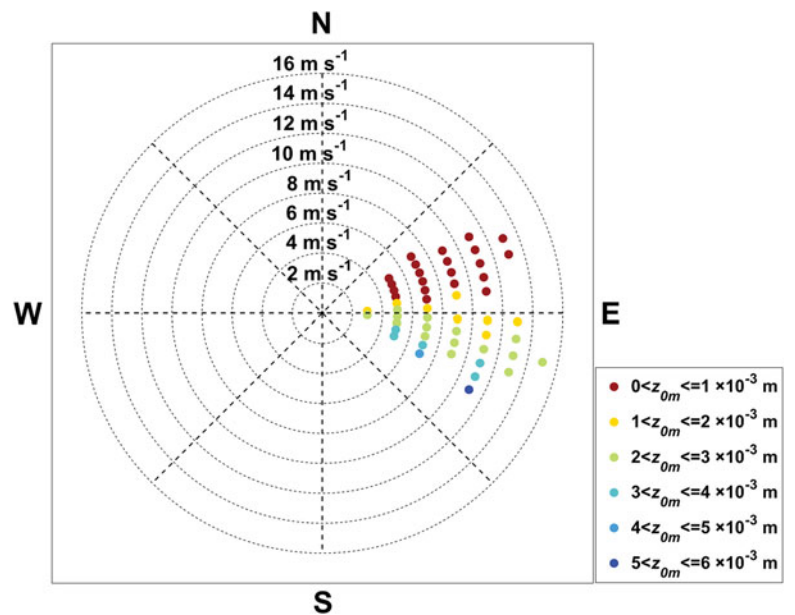
Month	NSR ( $W m^{-2}$ )	NLR ( $W m^{-2}$ )	$R_n$ ( $W m^{-2}$ )	$SH$ ( $W m^{-2}$ )	$LE$ ( $W m^{-2}$ )
May (November)	1 (0)	-46 (-17)	-46 (-17)	29 (2)	-11 (0)
June (December)	0 (0)	-40 (-33)	-40 (-33)	22 (6)	-8 (0)
July (January)	0 (0)	-26 (-26)	-26 (-26)	25 (6)	-6 (0)
August (February)	3 (0)	-58 (-29)	-58 (-29)	43 (9)	-13 (0)
September (March)	11 (6)	-47 (-16)	-36 (-10)	36 (3)	-12 (0)
October (April)	36 (22)	-53 (-22)	-17 (0)	21 (0)	-13 (0)
November (May)	91 (42)	-69 (-27)	21 (15)	26 (-1)	-32 (-4)

Figure 7 describes the monthly variation of the surface energy budget. From April to October, ice surface lost energy through  $R_n$  and  $LE$  while obtained energy through  $SH$  and  $G$ , and  $SH$  was the main heat source of surface from July to October. On the other hand, the small negative  $F_{net}$  appeared during the sea-ice growth period, and the mean value of  $F_{net}$  from April to October was  $-7 W m^{-2}$ . However, in November, the distinctly negative  $LE$  was the only heat sink of surface and  $F_{net}$  turned to positive. The surplus energy was used for surface warming or melting as the surface temperature was first observed to reach  $0^\circ C$  on 1 November.

To better understand the differences in snow or sea-ice processes, related to surface heat fluxes, between the Antarctica and the Arctic, two Arctic field experiments, included the Surface Heat Budget of the Arctic Ocean (SHEBA) and N-ICE2015 (a campaign focused on the surface energy budget over young, thin Arctic sea ice), were compared with our observation results. The statistics of SHEBA and N-ICE2015 were concluded from Persson and others (2002) and Walden and others (2017). The monthly mean values of net shortwave radiation (NSR hereafter,  $NSR = S_{\downarrow} - S_{\uparrow}$ ), net longwave radiation (NLR hereafter,  $NLR = L_{\downarrow} - L_{\uparrow}$ ),  $R_n$ ,  $SH$  and  $LE$  from May to November (from November to May in SHEBA) were shown in Table 3. From May to August, the monthly mean NSR from our observation and SHEBA both were close to zero, surface radiation budget was dominated by longwave radiation. While, the monthly mean NSR in our observation was larger than that in SHEBA from September to November, because the location of SHEBA observation site was

at higher latitudes ( $76-77^\circ N$ ). The NLR in our observation and SHEBA both were negative, which meant that surface lost energy through longwave radiation. In fact, the values of  $L_{\downarrow}$  and  $L_{\uparrow}$  both were larger in our observation, but the difference of  $L_{\downarrow}$  between our observation and SHEBA was greater than that of  $L_{\uparrow}$  in most months, which further lead to the larger negative NLR in our observation. However, the energy loss by NLR in July was the smallest in our observation and was equal to that in SHEBA, due to the frequent heavy precipitation events, which enhanced  $L_{\downarrow}$ .  $R_n$  was controlled by NSR and NLR, and showed the same direction but larger magnitude in our observation compared to that in SHEBA. Compared with the results of SHEBA, although the increase of  $L_{\downarrow}$  in our observation was greater than the increase of  $L_{\uparrow}$ , the increase of air temperature was still greater than that of surface temperature because the effective longwave emissivity of the Polar atmosphere was much smaller than the emissivity of sea-ice surface. Therefore, the inversion temperature gradient in our observation was stronger, the stratification was more stable and the downward sensible heat flux was larger. In contrast to our results, the contribution of  $LE$  in surface heat budget in SHEBA were negligible, because the air was drier and the higher wind speed was conducive to evaporation in our observation.

In a winter case study of N-ICE2015 campaign, the values of  $R_n$  and  $SH$  were comparable to our results under clear skies and showed a larger magnitude than SHEBA. Graham and others (2017) attributed the differences between two Arctic experiments to the geographical location. The N-ICE2015 site was located



**Fig. 8.** Distribution of  $z_{0m}$  under various wind speed and wind direction (the results were shown only when the number of sample in each bin is  $>5$ ).

close to the ice edge, where it allowed stronger winds and more advection of heat, but the SHEBA camp was located far from the ice edge. However,  $R_n$  was near to  $0 \text{ W m}^{-2}$  and  $SH$  could reach  $-50 \text{ W m}^{-2}$  during N-ICE2015 when the storm events occurred, due to the cloud over and cold air advection.

### 3.4 Roughness lengths

#### 3.4.1 Aerodynamic roughness length $z_{0m}$

The aerodynamic roughness length  $z_{0m}$  is an essential parameter in the calculation of turbulent fluxes by Bulk method. Under near-neutral condition ( $-0.01 \leq \zeta \leq 0.01$ ), Eqn (9) is written as,

$$z_{0m} = z / \exp\left(\frac{uk}{u_*}\right), \quad (24)$$

then  $z_{0m}$  can be calculated with measured  $u_*$  by EC method and wind speed  $u$ . It is found that large values of  $z_{0m}$  were concentrated in the direction of ESE to ES, while small values in NE to E (Fig. 8). However, there was no significant correlation between  $z_{0m}$  and wind speed. Such a distribution of  $z_{0m}$  might be caused by the orientation of surface undulating (e.g. Vignon and others, 2017). Our results indicate that the all-averaged value of  $z_{0m}$  was  $1.9 \times 10^{-3} \text{ m}$ , with a range of uncertainty from  $2.2 \times 10^{-4} \text{ m}$  to  $5.4 \times 10^{-3} \text{ m}$ . This coincides reasonably well with the typical range of order of magnitude of  $z_{0m}$ ,  $1 \times 10^{-4} \text{ m}$  to  $1 \times 10^{-2} \text{ m}$  (Guest and Davidson, 1991), for the Antarctic sea-ice/snow surface. However, Andreas (2011) pointed out that  $z_{0m}$  might be a site-dependent parameter, which depending on the surface elevation along upwind lines.

By analyzing the roughness of the snow-covered surface in the ablation zone of a Greenland ice sheet in the Arctic, Smeets and Van den Broeke (2008a) concluded that melting snow could increase  $z_{0m}$ . Here, we calculated the mean value of  $z_{0m}$  by using the data before 1 November and after 1 November (when the surface temperature started to rise above  $0^\circ\text{C}$ ), and the corresponding values were  $1.8 \times 10^{-3} \text{ m}$  and  $2.2 \times 10^{-3} \text{ m}$ , respectively. Hence, our results also showed that the aerodynamic roughness slightly increased due to snow melting. Unfortunately, the absence of summer observation prevented us from drawing a clear seasonal variation of  $z_{0m}$ . In fact, from the results of Wamser and Martinson (1993) and Weiss and others (2011), it can be found that the value of  $z_{0m}$  for multiyear pack ice in

Weddell Sea in summer ( $4.1 \times 10^{-3} \text{ m}$ ) was of order of magnitude larger than in winter ( $4.7 \times 10^{-4} \text{ m}$ ).

#### 3.4.2 Scalar roughness length for temperature $z_{0h}$

Based on the MOST,  $z_{0h}$  can be calculated by Eqn (10) and (12) with measured  $u_*$ ,  $T_*$  and established stability correction functions. Figure 9 compares several popular parameterization schemes of  $\log(z_{0h}/z_{0m})$ . It can be found that data were mainly concentrated on the range of  $\log(Re_*)$  from 2.5 to 5, corresponding to the rough surface. For the region of  $2.5 < \log(Re_*) < 5$ , it is clear that A87 scheme made a good performance in the calculation of  $\log(z_{0h}/z_{0m})$ , while other schemes all overestimated significantly. However, when  $\log(Re_*) \leq 2.5$ , the bias and normalized standard error (NSE) of  $SH$  parameterized by Bulk method with C97 scheme were smallest (Table 4). The overall averaged  $\log(z_{0h}/z_{0m}) = -3.93$ , which makes  $z_{0h} = 3.7 \times 10^{-5} \text{ m}$ . This value is two orders of magnitude lower than the value of  $8 \times 10^{-3} \text{ m}$  obtained by Cassano and others (2001) at Halley Research Station, but on the same order of magnitude as the value of  $2.9 \times 10^{-5} \text{ m}$  at the west western part of Queen Maud Land, Antarctica, suggested by Bintanja and Van den Broeke (1995) or the value of  $2.0 \times 10^{-5} \text{ m}$  found at Dome C, Antarctica, by Vignon and others (2017).

Large and others (1994) reported that  $z_{0h}$  existed considerable differences in orders of magnitude between unstable and stable stratification over the open ocean. Then, Andreas and others (2010) first considered the stratification dependence of  $z_{0h}$  over sea ice. They found that the values of  $\log(z_{0h}/z_{0m})$  were larger under unstable stratification than under stable stratification by analyzing the data collected during SHEBA experiments, but they did not think the statistical results were enough conclusive. In this study, the mean value of  $\log(z_{0h}/z_{0m})$  under stable ( $\zeta > 0.01$ ), near-neutral ( $-0.01 \leq \zeta \leq 0.01$ ) and unstable ( $\zeta < -0.01$ ) stratification were  $-3.48$ ,  $-5.01$  and  $-1.20$ , respectively. However, because the amount of data under unstable stratification is too small to be convincing, the mean value of  $\log(z_{0h}/z_{0m})$  under unstable stratification is not discussed. Our results show that  $\log(z_{0h}/z_{0m})$  was larger under stable stratification than under near-neutral stratification and the significant difference has been proved through the Student's  $t$  test with 95% statistical confidence. A possible explanation is that, under near-neutral stratification, the stronger wind speed leads to the larger  $Re_*$  and the increase of  $Re_*$  will decrease  $\log(z_{0h}/z_{0m})$  according to

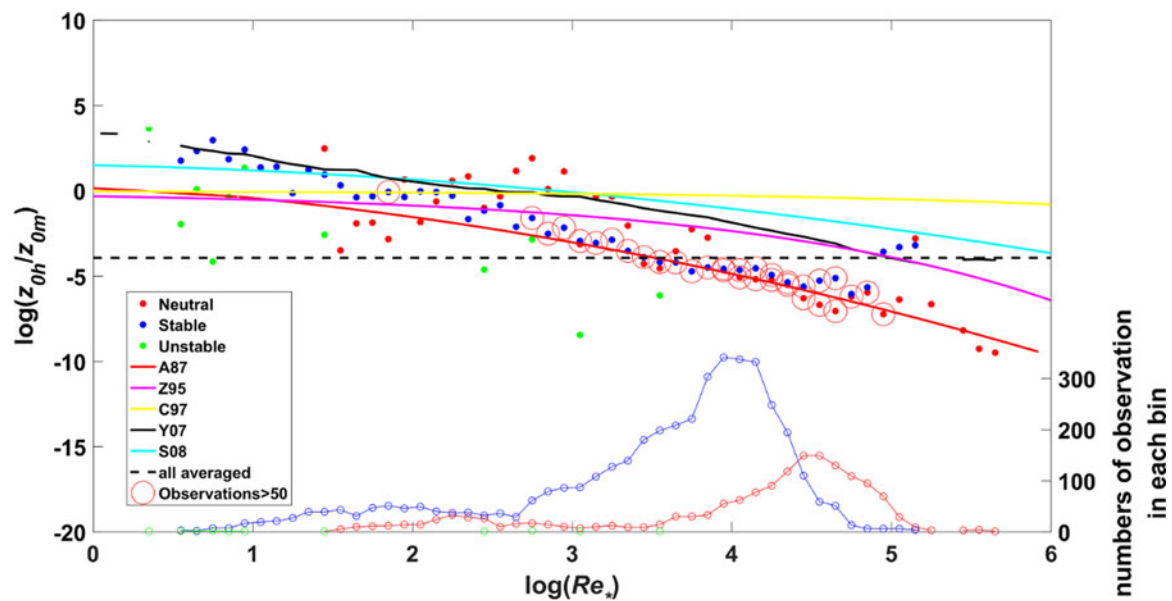


**Fig. 9.** The calculated  $\log(z_{0h}/z_{0m})$  versus  $\log(Re_*)$ . The dots are the bin averaged  $\log(z_{0h}/z_{0m})$  with 0.1 interval of  $\log(Re_*)$  and red, blue and green colors represent for neutral, stable and unstable condition, respectively. Red circles indicate that the observation sample number in the bin is larger than 50. The red solid line, mauve solid line, yellow solid line, black solid line, cyan solid line and black dashed line are  $\log(z_{0h}/z_{0m})$  from A87, Z95, C97, Y07, S08 and whole averaged of original data, respectively. The sample numbers of neutral (red dot-dashed line), stable (blue dot-dashed line), and unstable (green dot-dashed line) condition in each bin are shown in the bottom part.

**Table 4.** The regression slope, bias, and NSE of SH parameterized by Bulk method with various  $z_{0h}$  schemes in the different region of  $\log(Re_*)$

Region	Sample number	Scheme	Regression slope	Bias ( $W m^{-2}$ )	NSE
$\log(Re_*) \leq 2.5$	880	A87	0.83	4.2	0.28
		Z95	0.87	4.0	0.26
		C97	0.94	<b>3.9</b>	<b>0.25</b>
		Y07	<b>0.98</b>	4.3	0.28
		S08	<b>1.02</b>	4.1	0.27
$\log(Re_*) > 2.5$	5057	A87	<b>0.94</b>	<b>5.4</b>	<b>0.20</b>
		Z95	1.2	9.5	0.31
		C97	1.58	21.0	0.67
		Y07	1.21	10.7	0.34
		S08	1.39	15.4	0.48

Boldface numbers are the best among these schemes. Here, bias =  $\sum_{i=1}^n |SH_{EC} - SH_{Bulk}|/n$  and NSE =  $\sqrt{\frac{\sum_{i=1}^n |SH_{EC} - SH_{Bulk}|^2}{\sum_{i=1}^n |SH_{EC}|^2}}$ .

Andreas (1987). From Figure 9, we can also find that the data under near-neutral stratification were concentrated on the large  $Re_*$  region.

#### 4. Conclusions

By using the data observed over sea-ice surface near Zhongshan station during the period from 8 April 2016 through 26 November 2016, this study focuses on the status of surface energy budget and the crucial parameters,  $z_{0m}$  and  $z_{0h}$ , in the parameterization of turbulent fluxes, and we conclude the following:

During the whole observation period, the mean (4-hour-averaged maximum/minimum) wind speed and air temperature at 2 m height, and surface temperature were 4.2 (13.9/0)  $m s^{-1}$ ,  $-15$  (3/−40)°C and  $-17$  (2/−48)°C, respectively. In November, caused by the influence of local sea breeze, wind speed (wind direction) showed a significant daily variation. July (November) was the wettest (driest) month. The accumulated precipitation during the observation was 156.9 mm and concentrated in July. The monthly mean albedo decreased from 0.93 in July to 0.69 in November, which related to the snow melting process.

From April to October, most of the lost surface energy through  $LE$  and  $R_n$  was balanced by  $SH$  and  $G$ , and  $F_{net}$  was slightly negative.

However,  $LE$  was the only heat sink of surface and  $F_{net}$  turned to positive in November. The direction of energy fluxes in our study was generally consistent with previous studies both in the Antarctica and Arctic, but showed differences in magnitude. Our results support that the strong winds in the katabatic wind zone enhance the downward  $SH$  in Antarctica. Additionally, two Arctic experiments were compared with our observation. The results from SHEBA data showed smaller positive  $SH$  (negative  $LE$ ), due to the colder air (wetter air and lower wind speed). While, the values of  $R_n$  and  $SH$  in N-ICE2015 campaign were comparable to our results under clear skies, but  $SH$  turned to negative caused by the effects of cloud over and cold air advection during the storm events.

In this study, the mean value of  $z_{0m}$  was  $1.9 \times 10^{-3}$  m. It is found that  $z_{0m}$  did not vary with wind speed but changed with wind direction and snow melting might increase  $z_{0m}$ . Meanwhile, the all-averaged value of  $z_{0h}$ , being  $3.7 \times 10^{-5}$  m, was suggested in our study. Our results showed that the parameterization scheme of  $z_{0h}$  proposed by Andreas (1987) made a better performance in the region of  $\log(Re_*) > 2.5$  and Chen and others (1997)'s scheme was more reasonable when  $\log(Re_*) \leq 2.5$ . Additionally, the larger value of  $\log(z_{0h}/z_{0m})$  was found under stable stratification than under near-neutral stratification, due to the stronger winds under near-neutral stratification.

Although we have presented some observation results and analysis for surface energy budget and parameterization of near-surface turbulent fluxes over the Antarctic sea ice, the work of evaluating the numerical model [e.g. HIGHTSI model (a high-resolution thermodynamic snow and ice model)] has not been done at present, and this will be carried out in the future.

**Acknowledgements.** This work was jointly supported by the National Key Projects of Ministry of Science and Technology of China (2016YFA0602100), the Foundation of Key Laboratory of Land Surface Process and Climate Change in Cold and Arid Regions (LPCC2018001, LPCC2018005), the National Natural Science Foundation of China (41875013, 41941009, 41675015), the Fundamental Research Funds for the Central Universities (No. 19lgzd07), the Key Research Program of Frontier Sciences of CAS (QYZDY-SSW-DQC021), the Opening fund of State Key Laboratory of Cryospheric Science (SKLCS-OP-2019-09), and the Postgraduate Research & Practice Innovation Program of Jiangsu Province (KYCX18\_1006). This is a contribution to the Year of Polar Prediction (YOPP), a flagship activity of the Polar Prediction Project (PPP), initiated by the World Weather Research Programme (WWRP) of the World Meteorological Organization (WMO). We thank the Chinese Arctic and Antarctic Administration and Polar Research Institute of China for the logistic support. We also thank the Russian meteorological station of Progress for providing precipitation data.

**Author contributions.** Changwei Liu performed most calculations and wrote the first version of the paper, Zhiqiu Gao made many constructive suggestions and helped improve the manuscript, Qinghua Yang provided most of the data and also participated in revising the manuscript, Bo Han, Hong Wang, Linlin Wang and Yubin Li helped revise the manuscript, Guanghua Hao, Jiechen Zhao and Lejiang Yu collected the data and conducted some calculations.

## References

- Andreas EL (1987) A theory for the scalar roughness and the scalar transfer coefficients over snow and sea ice. *Boundary-Layer Meteorology* **38**(1), 159–184. doi: [10.1007/BF00121562](https://doi.org/10.1007/BF00121562).
- Andreas EL and 6 others (2010) Parameterizing turbulent exchange over sea ice in winter. *Journal of Hydrometeorology* **11**(1), 87–104. doi: [10.1175/2009JHM1102.1](https://doi.org/10.1175/2009JHM1102.1).
- Andreas EL (2011) A relationship between the aerodynamic and physical roughness of winter sea ice. *Quarterly Journal of the Royal Meteorological Society* **137**(659), 1581–1588. doi: [10.1002/qj.842](https://doi.org/10.1002/qj.842).
- Andreas EL, Tucker III WB and Ackley SF (1984) Atmospheric boundary-layer modification, drag coefficient, and surface heat flux in the Antarctic marginal ice zone. *Journal of Geophysical Research: Oceans* **89**(C1), 649–661. doi: [10.1029/JC089iC01p00649](https://doi.org/10.1029/JC089iC01p00649).
- Bintanja R and Van den Broeke MR (1995) Momentum and scalar transfer coefficients over aerodynamically smooth Antarctic surface. *Boundary-Layer Meteorology* **74**(1), 89–111. doi: [10.1007/BF00715712](https://doi.org/10.1007/BF00715712).
- Bourassa MA and 16 others (2013) High-Latitude ocean and sea ice surface fluxes: challenges for climate research. *Bulletin of the American Meteorological Society* **94**(3), 403–423. doi: [10.1175/BAMS-D-11-00244.1](https://doi.org/10.1175/BAMS-D-11-00244.1).
- Brunke MA, Zhou M, Zeng X and Andreas EL (2006) An intercomparison of bulk aerodynamic algorithms used over sea ice with data from the Surface Heat Budget for the Arctic Ocean (SHEBA) experiment. *Journal of Geophysical Research: Oceans* **111**(C9), C09001. doi: [10.1029/2005JC002907](https://doi.org/10.1029/2005JC002907).
- Cassano JJ, Parish TR and King JC (2001) Evaluation of turbulent surface flux parameterizations for the stable surface layer over Halley, Antarctica\*. *Monthly Weather Review* **129**(1), 26–46. doi: [10.1175/1520-0493\(2001\)129%3C0026:EOTSFP%3E2.0.CO;2](https://doi.org/10.1175/1520-0493(2001)129%3C0026:EOTSFP%3E2.0.CO;2).
- Chen F, Janjić Z and Mitchell K (1997) Impact of atmospheric surface-layer parameterizations in the new land-surface scheme of the NCEP mesoscale Eta model. *Boundary-Layer Meteorology* **85**(3), 391–421. doi: [10.1023/A:1000531001463](https://doi.org/10.1023/A:1000531001463).
- Cheng Y and Brutsaert W (2005) Flux-profile relationships for wind speed and temperature in the stable atmospheric boundary layer. *Boundary-Layer Meteorology* **114**(3), 519–538. doi: [10.1007/s10546-004-1425-4](https://doi.org/10.1007/s10546-004-1425-4).
- Cullen N, Mölg T, Kaser G, Steffen K and Hardy D (2007) Energy-balance model validation on the top of Kilimanjaro, Tanzania, using eddy covariance data. *Annals of Glaciology* **46**(1), 227–233. doi: [10.3189/172756407782871224](https://doi.org/10.3189/172756407782871224).
- Else BGT and 7 others (2014) Surface energy budget of landfast sea ice during the transitions from winter to snowmelt and melt pond onset: the importance of the net longwave radiation and cyclone forcings. *Journal of Geophysical Research: Oceans* **119**, 3679–3693. doi: [10.1002/2013JC009672](https://doi.org/10.1002/2013JC009672).
- Foken T, Leuning R, Oncley SR, Mauder M and Aubinet M (2012) Corrections and data quality control. In Aubinet M, Vesala T and Papale D (eds), *Eddy Covariance: A Practical Guide to Measurement and Data Analysis*. New York: Springer, pp. 85–131.
- Garratt JR (1992) *The Atmospheric Boundary Layer*. Cambridge, UK: Cambridge University Press, pp. 316.
- Grachev AA, Andreas EL, Fairall CW, Guest PS and Persson POG (2007) SHEBA flux–profile relationships in the stable atmospheric boundary layer. *Boundary-Layer Meteorology*, **124**(3), 315–333. doi: <http://dx.doi.org/10.1007/s10546-007-9177-6>.
- Grachev AA, Andreas EL, Fairall CW, Guest PS and Persson POG (2013) The critical Richardson number and limits of applicability of local similarity theory in the stable boundary layer. *Boundary-Layer Meteorology* **147**(1), 51–82. doi: [10.1007/s10546-012-9771-0](https://doi.org/10.1007/s10546-012-9771-0).
- Graham RM and 8 others (2017) A comparison of the two Arctic atmospheric winter states observed during N-ICE2015 and SHEBA. *Journal of Geophysical Research: Atmospheres* **122**, 5716–5737. doi: [10.1002/2016JD025475](https://doi.org/10.1002/2016JD025475).
- Guest PS and Davidson KL (1991) The aerodynamic roughness of different types of sea ice. *Journal of Geophysical Research: Oceans* **96**(C3), 4709–4721. doi: [10.1029/90JC02261](https://doi.org/10.1029/90JC02261).
- Guo X and 7 others (2011) Critical evaluation of scalar roughness length parametrizations over a melting valley glacier. *Boundary-Layer Meteorology* **139**(2), 307–332. doi: [10.1007/s10546-010-9586-9](https://doi.org/10.1007/s10546-010-9586-9).
- King JC (1990) Some measurements of turbulence over an Antarctic ice shelf. *Quarterly Journal of the Royal Meteorological Society* **116**(492), 379–400. doi: [10.1002/qj.49711649208](https://doi.org/10.1002/qj.49711649208).
- King JC and Anderson PS (1994) Heat and water vapour fluxes and scalar roughness lengths over an Antarctic ice shelf. *Boundary-Layer Meteorology* **69**(1-2), 101–121. doi: [10.1007/BF00713297](https://doi.org/10.1007/BF00713297).
- King JC, Anderson PS, Smith MC and Mobbs SD (1996) The surface energy and mass balance at Halley, Antarctica during winter. *Journal of Geophysical Research* **101**(D14), 119–128. doi: [10.1029/96JD01714](https://doi.org/10.1029/96JD01714).
- King JC, Connolley WM and Derbyshire SH (2001) Sensitivity of modelled Antarctic climate to surface and boundary-layer flux parametrizations. *Quarterly Journal of the Royal Meteorological Society* **127**(573), 779–794. doi: [10.1002/qj.49712757304](https://doi.org/10.1002/qj.49712757304).
- King JC, Varley MJ and Lachlan-Cope TA (1998) Using satellite thermal infrared imagery to study boundary-layer structure in an Antarctic katabatic wind region. *International Journal of Remote Sensing* **19**(17), 3335–3348. doi: [10.1080/014311698214028](https://doi.org/10.1080/014311698214028).
- Kljun N, Calanca P, Rotach MW and Schmid HP (2015) The simple two-dimensional parameterisation for Flux Footprint Predictions (FFP). *Geoscientific Model Development* **8**(8), 6757–6808. doi: [10.5194/gmd-8-3695-2015](https://doi.org/10.5194/gmd-8-3695-2015).
- Large WG, Mc Williams JC and Doney SC (1994) Sensible and latent heat flux measurements over the ocean. *Journal of Physical Oceanography* **12**(5), 464–482. doi: [10.1175/1520-0485\(1982\)012<0464:SALHFM>2.0.CO;2](https://doi.org/10.1175/1520-0485(1982)012<0464:SALHFM>2.0.CO;2).
- Lazzara MA, Weidner GA, Keller LM, Thom JE and Cassan JJ (2012) Antarctic automatic weather station program: 30 years of Polar observation. *Bulletin of the American Meteorological Society* **93**(10), 1519–1537. doi: [10.1175/BAMS-D-11-00015.1](https://doi.org/10.1175/BAMS-D-11-00015.1).
- Lee X, Massman W and Law B (2004) *Handbook of Micrometeorology: A Guide for Surface Flux Measurement and Analysis*. Dordrecht: Kluwer Academic Publisher, pp. 119–160.
- Liu C and 6 others (2019) On the surface fluxes characteristics and roughness lengths at Zhongshan station, Antarctica. *International Journal of Digital Earth*, **12**(8), 878–892. doi: [10.1080/17538947.2017.1335804](https://doi.org/10.1080/17538947.2017.1335804).
- Munro DS (1989) Surface roughness and bulk heat transfer on a glacier: comparison with eddy correlation. *Journal of Glaciology* **35**(121), 343–348. doi: [10.1017/S002214300009266](https://doi.org/10.1017/S002214300009266).
- Paulson CA (1970) The mathematical representation of wind speed and temperature profiles in the unstable atmospheric surface layer. *Journal of Applied Meteorology and Climatology* **9**(9), 857–861. doi: [10.1175/1520-0450\(1970\)009<0857:TMROWS>2.0.CO;2](https://doi.org/10.1175/1520-0450(1970)009<0857:TMROWS>2.0.CO;2).

- Perovich DK, Grenfell TC, Light B and Hobbs PV** (2002) Seasonal evolution of the albedo of multiyear Arctic sea ice. *Journal of Geophysical Research* **107**(C10), 8044. doi: [10.1029/2000JC000438](https://doi.org/10.1029/2000JC000438).
- Perovich DK and Polashenski C** (2012) Albedo evolution of seasonal Arctic sea ice. *Geophysical Research Letters* **39**(8), L08501. doi: [10.1029/2012GL051432](https://doi.org/10.1029/2012GL051432).
- Persson POG, Fairall CW, Andreas EL, Guest PS and Perovic DK** (2002) Measurements near the Atmospheric Surface Flux Group tower at SHEBA: near-surface conditions and surface energy budget. *Journal of Geophysical Research* **107**(C10), 8045. doi: [10.1029/2000JC000705](https://doi.org/10.1029/2000JC000705).
- Reijmer CH, Meijgaard EV and Van den Broeke MR** (2003) Roughness length for momentum and heat over Antarctica in a regional atmospheric climate model. In Proceedings of the seventh conference on Polar meteorology and oceanography and joint symposium on high-latitude climate variations, Hyannis, Massachusetts. Washington, DC, American Meteorological Society. CD-ROM, May 12-16.
- Rigden A, Li D and Salvucci G** (2018) Dependence of thermal roughness length on friction velocity across land cover types: a synthesis analysis using AmeriFlux data. *Agricultural and Forest Meteorology* **249**, 512–519. doi: [10.1016/j.agrformet.2017.06.003](https://doi.org/10.1016/j.agrformet.2017.06.003).
- Rodrigo JS and Anderson PS** (2013) Investigation of the stable atmospheric boundary layer at Halley Antarctica. *Boundary-Layer Meteorology* **148**(3), 517–539. doi: [10.1007/s10546-013-9831-0](https://doi.org/10.1007/s10546-013-9831-0).
- Schröder D, Vihma T, Kerber A and Brümmner B** (2003) On the parameterization of turbulent surface fluxes over heterogeneous sea ice surfaces. *Journal of Geophysical Research*, **108**(C6). doi: <http://dx.doi.org/10.1029/2002JC001385>.
- Smeets CJPP and Van den Broeke MR** (2008a) Temporal and spatial variation of momentum roughness length in the ablation zone of the Greenland ice sheet. *Boundary-Layer Meteorology* **128**(3), 315–338. doi: [10.1007/s10546-008-9291-0](https://doi.org/10.1007/s10546-008-9291-0).
- Smeets CJPP and Van den Broeke MR** (2008b) The parameterization of scalar transfer over rough ice. *Boundary-Layer Meteorology* **128**(3), 339–355. doi: [10.1007/s10546-008-9292-z](https://doi.org/10.1007/s10546-008-9292-z).
- Stearns CR and Weidner GA** (1993) *Sensible and latent heat flux estimates in Antarctica*. Antarctic meteorology and climatology: studies based on automatic weather stations, American Geophysical Union, Washington, 109–138
- Sun J** (1999) Diurnal variations of thermal roughness height over a grassland. *Boundary-Layer Meteorology* **92**(3), 407–427. doi: [10.1023/A:1002071421362](https://doi.org/10.1023/A:1002071421362).
- Toyota T, Massom R, Tateyama K, Tamura T and Fraser A** (2011) Properties of snow overlying the sea ice off East Antarctica in late winter, 2007. *Deep-Sea Research Part II* **58**(9–10), 1137–1148. doi: [10.1016/j.dsr2.2010.12.002](https://doi.org/10.1016/j.dsr2.2010.12.002).
- Van den Broeke MR, van As D, Reijmer C and van de Wal R** (2005) Sensible heat exchange at the Antarctic snow surface: a study with automatic weather stations. *International Journal of Climatology* **25**(8), 1081–1101. doi: [10.1002/joc.1152](https://doi.org/10.1002/joc.1152).
- Vignon E and 7 others** (2017) Momentum- and heat-flux parametrization at Dome C, Antarctica: a sensitivity study. *Boundary-Layer Meteorology* **162**(2), 1–27. doi: [10.1007/s10546-016-0192-3](https://doi.org/10.1007/s10546-016-0192-3).
- Vihma T, Johansson MM and Launiainen J** (2009) Radiative and turbulent surface heat fluxes over sea ice in the western Weddell Sea in early summer. *Journal of Geophysical Research: Oceans* **114**(C4), C04019. doi: [10.1029/2008JC004995](https://doi.org/10.1029/2008JC004995).
- Walden VP, Hudson SR, Cohen L, Murphy SY and Granskog MA** (2017) Atmospheric components of the surface energy budget over young sea ice: results from the N-ICE2015 campaign. *Journal of Geophysical Research: Atmospheres* **122**(16), 8427–8446. doi: [10.1002/2016JD026091](https://doi.org/10.1002/2016JD026091).
- Wamser C and Martinson DG** (1993) Drag coefficients for winter Antarctic peak ice. *Journal of Geophysical Research: Oceans* **98**(C7), 12431–12437. doi: [10.1029/93JC00655](https://doi.org/10.1029/93JC00655).
- Weiss AI, King J, Lachlan-Cope T and Ladkin R** (2011) On the effective aerodynamic and scalar roughness length of Weddell sea ice. *Journal of Geophysical Research: Atmospheres* **116**(D19), D19119. doi: [10.1029/2011JD015949](https://doi.org/10.1029/2011JD015949).
- Wendler G, Moore B, Dissing D and Kelley J** (2000) On the radiation characteristics of Antarctic Sea Ice. *Atmosphere-Ocean* **38**(2), 349–366. doi: [10.1080/07055900.2000.9649652](https://doi.org/10.1080/07055900.2000.9649652).
- Yagüe C and Cano JL** (1994) The influence of stratification on heat and momentum turbulent transfer in Antarctica. *Boundary-Layer Meteorology* **69**(1–2), 123–136. doi: [10.1007/BF00713298](https://doi.org/10.1007/BF00713298).
- Yang K and 8 others** (2007) Turbulent flux transfer over bare-soil surfaces: characteristics and parameterization. *Journal of Applied Meteorology and Climatology* **47**(1), 276–290. doi: [10.1175/2007JAMC1547.1](https://doi.org/10.1175/2007JAMC1547.1).
- Yang Q and 11 others** (2016) Albedo of coastal landfast sea ice in Prydz Bay, Antarctica: observations and parameterization. *Advances in Atmospheric Sciences* **33**, 535–543. doi: [10.1007/s00376-015-5114-7](https://doi.org/10.1007/s00376-015-5114-7).
- Yang K, Koike T, Fujii H, Tamagawa K and Hirose N** (2002) Improvement of surface flux parametrizations with a turbulence-related length. *Quarterly Journal of the Royal Meteorological Society* **128**(584), 2073–2087. doi: [10.1256/003590002320603548](https://doi.org/10.1256/003590002320603548).
- Yu L and 9 others** (2019) The variability of surface radiation fluxes over landfast sea ice near Zhongshan station, East Antarctica during austral spring. *International Journal of Digital Earth*, **12**(8), 860–877. doi: [10.1080/17538947.2017.1304458](https://doi.org/10.1080/17538947.2017.1304458).
- Zilitinkevich SS** (1995) *Non-Local Turbulent Transport: Pollution Dispersion Aspects of Coherent Structure of Convective Flows*. Air Pollution Theory and Simulation, Computational Mechanics Publications, Southampton, Boston, 53–60